



This is a repository copy of *Millimeter-scale unipolar transport in high sensitivity organic-inorganic semiconductor X-Ray detectors.*

White Rose Research Online URL for this paper:
<http://eprints.whiterose.ac.uk/146724/>

Version: Accepted Version

Article:

Jayawardena, K.D.G.I., Thirimanne, H.M., Tedde, S.F. et al. (5 more authors) (2019) Millimeter-scale unipolar transport in high sensitivity organic-inorganic semiconductor X-Ray detectors. ACS Nano. ISSN 1936-0851

<https://doi.org/10.1021/acsnano.9b01916>

This document is the Accepted Manuscript version of a Published Work that appeared in final form in ACS Nano, copyright © American Chemical Society after peer review and technical editing by the publisher. To access the final edited and published work see <https://doi.org/10.1021/acsnano.9b01916>

Reuse

Items deposited in White Rose Research Online are protected by copyright, with all rights reserved unless indicated otherwise. They may be downloaded and/or printed for private study, or other acts as permitted by national copyright laws. The publisher or other rights holders may allow further reproduction and re-use of the full text version. This is indicated by the licence information on the White Rose Research Online record for the item.

Takedown

If you consider content in White Rose Research Online to be in breach of UK law, please notify us by emailing eprints@whiterose.ac.uk including the URL of the record and the reason for the withdrawal request.



eprints@whiterose.ac.uk
<https://eprints.whiterose.ac.uk/>

Millimeter-Scale Unipolar Transport in High Sensitivity Organic-Inorganic Semiconductor X-Ray Detectors

K. D. G. Imalka Jayawardena, Hashini M. Thirimanne, Sandro Francesco Tedde, Judith E. Huerdler, Andrew J. Parnell, R. M. Indrachapa Bandara, Christopher A. Mills, and S. Ravi P. Silva

ACS Nano, **Just Accepted Manuscript** • DOI: 10.1021/acsnano.9b01916 • Publication Date (Web): 24 May 2019

Downloaded from <http://pubs.acs.org> on May 31, 2019

Just Accepted

“Just Accepted” manuscripts have been peer-reviewed and accepted for publication. They are posted online prior to technical editing, formatting for publication and author proofing. The American Chemical Society provides “Just Accepted” as a service to the research community to expedite the dissemination of scientific material as soon as possible after acceptance. “Just Accepted” manuscripts appear in full in PDF format accompanied by an HTML abstract. “Just Accepted” manuscripts have been fully peer reviewed, but should not be considered the official version of record. They are citable by the Digital Object Identifier (DOI®). “Just Accepted” is an optional service offered to authors. Therefore, the “Just Accepted” Web site may not include all articles that will be published in the journal. After a manuscript is technically edited and formatted, it will be removed from the “Just Accepted” Web site and published as an ASAP article. Note that technical editing may introduce minor changes to the manuscript text and/or graphics which could affect content, and all legal disclaimers and ethical guidelines that apply to the journal pertain. ACS cannot be held responsible for errors or consequences arising from the use of information contained in these “Just Accepted” manuscripts.

1
2
3
4
5
6
7
8
9
10
11
12
13
14
15
16
17
18
19
20
21
22
23
24
25
26
27
28
29
30
31

Millimeter-Scale Unipolar Transport in High Sensitivity Organic-Inorganic Semiconductor X-Ray Detectors

K. D. G. Imalka Jayawardena^{1†}, Hashini M. Thirimanne^{1†}, Sandro Francesco Tedde²,

Judith E. Huerdler², Andrew J. Parnell^β, R. M. Indrachapa Bandara¹, Christopher A.

Mills¹,

S. Ravi P. Silva^{1}*

- 32
33
34
35
36
37
38
39
40
41
42
43
44
45
46
47
48
49
50
51
52
53
54
55
56
57
58
59
60
1. Advanced Technology Institute, Department of Electrical and Electronic Engineering, University of Surrey, Guildford, Surrey, GU2 7XH, United Kingdom.
 2. Siemens Healthineers, Technology Center, Guenther-Scharowsky-Str. 1, 91058 Erlangen, Germany.
 3. Department of Physics and Astronomy, University of Sheffield, Hicks Building, Sheffield, S3 7RH, United Kingdom.

1
2
3
4
5
6
7
8 Corresponding Author
9

10
11 *E-mail: s.silva@surrey.ac.uk
12
13

14
15
16 †These authors contributed equally.
17
18
19

20 21 **ABSTRACT** 22 23

24
25
26 Hybrid inorganic-in-organic semiconductors are an attractive class of materials for
27
28
29 optoelectronic applications. Traditionally, the thicknesses of organic semiconductors are
30
31
32 kept below 1 micron due to poor charge transport in such systems. However, recent work
33
34
35 suggests that charge carriers in such organic semiconductors can be transported over
36
37
38 centimeter length scales opposing this view. In this work, a unipolar X-ray photoconductor
39
40
41 based on a bulk heterojunction architecture, consisting of poly(3-hexylthiophene), a C70
42
43
44 derivative and high atomic number bismuth oxide nanoparticles operating in the 0.1 – 1
45
46
47 mm thickness regime is demonstrated, having a high sensitivity of $\sim 160 \mu\text{CmGy}^{-1}\text{cm}^{-3}$.
48
49
50
51
52
53
54 The high performance enabled by hole drift lengths approaching a millimeter facilitates a
55
56
57
58
59
60

1
2
3 device architecture allowing a high fraction of the incident X-rays to be attenuated. An X-
4
5
6
7 ray imager is demonstrated with sufficient resolution for security applications such as
8
9
10 portable baggage screening at border crossings and public events and scalable medical
11
12
13
14 applications.
15
16
17
18
19
20
21
22

23 **KEYWORDS**

24
25
26
27
28 detectors, direct conversion, radiation, inorganics, organics
29
30
31
32
33
34
35
36
37
38
39
40
41
42
43
44
45
46
47
48
49

50 Due to their low cost and solution processible nature, organic semiconductors based
51
52
53 on conjugated polymers and small molecules have been proposed for energy harvesting
54
55
56
57
58
59
60

1
2
3 applications,¹⁻³ light emitting devices.⁴ In addition to the applications highlighted above,
4
5
6 organic semiconductor based devices as well as inorganic-organic hybrid devices are
7
8
9
10 gaining attention for the detection of ionizing radiation.^{5,6} The first reported inorganic
11
12
13
14 nanomaterials used for sensitization of organic semiconductor devices for ionizing
15
16
17 radiation can be traced to the work of Intaniwet *et al.*⁷ where bismuth oxide nanoparticles
18
19
20 (Bi₂O₃ NPs) were incorporated into a *p*-type poly(triaryl amine) matrix for detection of
21
22
23
24 ionizing radiation based on a mono-carrier device architecture. The versatility of the
25
26
27
28 concept was further examined through variation of the high atomic number (Z) NP and
29
30
31 the organic semiconductor used.⁸ In addition to the above developments, Büchele *et al.*⁶
32
33
34 demonstrated that the incorporation of gadolinium oxysulfide micro-particles into an
35
36
37
38 organic bulk heterojunction matrix consisting of poly(3-hexyothiophene) (P3HT) and [6,6]
39
40
41 - Phenyl-C71-butyric acid methyl ester (PCBM) can result in X-ray detector that enable
42
43
44
45 higher resolution imaging capabilities for medical applications extending beyond the
46
47
48
49 current market offerings based on amorphous silicon photodiodes coupled with a cesium
50
51
52 iodide scintillator. The importance of the hybrid inorganic-organic semiconductor systems
53
54
55
56 have also been exemplified in the recent work of Civatti *et al.*⁹ where the X-ray sensitivity
57
58
59
60

1
2
3 of a previously demonstrated 6,13-bis(triisopropylsilylethynyl)pentacene system¹⁰ was
4
5
6
7 enhanced by substitution of the silicon atom in organic semiconductor with germanium.
8
9
10 In addition to the above, there has also been significant interest in the utilization of
11
12
13 perovskite semiconductors as direct conversion ionization radiation detectors¹¹⁻¹³ due to
14
15
16
17 their high X-ray attenuation (as a result of their high average atomic numbers) and high
18
19
20 carrier mobilities that enable efficient charge extraction from thick devices (several
21
22
23
24 hundred of microns to millimeters) that is a pre-requisite to enable a fraction of the incident
25
26
27
28 X-rays to be attenuated.
29
30

31 Based on the insights from above developments, we reported a direct conversion X-ray
32
33
34 detector concept based on a ternary system comprising of P3HT, PCBM and Bi₂O₃ NPs.⁵
35
36
37
38 Unlike conventional hybrid device concepts where organic semiconductors are utilized
39
40
41 for detection of visible – near infrared photons, this device architecture utilized P3HT and
42
43
44
45 PCBM as carrier selective charge transport pathways for free carriers generated due to
46
47
48 the interaction between the X-rays and the Bi₂O₃ NPs. This enabled a number of benefits
49
50
51
52 including high X-ray sensitivities of $\sim 1.7 \text{ mCmGy}^{-1}\text{cm}^{-3}$ when irradiated using “soft” X-
53
54
55
56 rays and $\sim 30 \text{ } \mu\text{C mGy}^{-1}\text{cm}^{-3}$ under 6 MV “hard” X-rays. However, the thickness of the
57
58
59
60

1
2
3 devices were limited to $< 30 \mu\text{m}$ due to the limitations in the fabrication process used as
4
5
6
7 well as due to the prevailing state of knowledge (during the period over which the work
8
9
10 was carried out) on the inability for organic semiconductors to transport charge over
11
12
13 several hundreds of microns. The high sensitivity obtained with such thin films has critical
14
15
16 implications including: a much lower dose detectability which is of importance in dosimetry
17
18
19
20
21 (*e.g.*: assessing damage to regions surrounding the area of interest in radiotherapy).
22
23
24 However, the thin nature and the resulting low attenuation of X-rays has significant
25
26
27 negative impact for X-ray imaging where a high X-ray attenuation is required for improving
28
29
30
31 image quality.
32
33

34
35 Recently, Gélinas *et al.* has shown that photo-generated electrons and holes in organic
36
37
38 semiconductors are efficiently separated through delocalized states on the femtosecond
39
40
41 time scale¹⁴ which results in the performances typically observed for organic
42
43
44 photovoltaics. Furthermore, Burlingame *et al.* demonstrated that the resulting free carriers
45
46
47
48 generated can be transported over centimeter length scales,¹⁵ challenging previously
49
50
51 held views of short charge transport lengths in these systems. Such long transport lengths
52
53
54
55 are particularly attractive, especially in terms of the development of ionizing radiation
56
57
58
59
60

1
2
3 detectors where thick absorbers are preferred for maximum radiation attenuation.^{5,6}
4
5

6
7 Here, a highly sensitive X-ray photoconductor based on the integration of inorganic
8
9
10 nanoparticles in an organic bulk heterojunction matrix with hole drift lengths approaching
11
12
13 1 mm is demonstrated. These drift lengths which exceed those of organic single
14
15
16 crystals,¹⁶ enables photoconductor thicknesses approaching a millimeter and X-ray
17
18 sensitivities of $\sim 160 \mu\text{CmGy}^{-1}\text{cm}^{-3}$.
19
20
21
22
23
24
25
26
27

28 RESULTS & DISCUSSION

31 Dose rate and thickness dependency of X-ray photocurrent response

32
33
34
35
36 The X-ray photoconductor developed in this work is based on P3HT as a p -type
37
38 semiconductor, PCBM as an electron trap and Bi_2O_3 NPs as the X-ray attenuator and a
39
40 route for free carrier generation (Figure 1a). The use of PCBM as an electron transporter,
41
42
43 as detailed in our previous work⁵ was avoided due to the lower electron mobilities
44
45
46 generally observed in fullerene systems.¹⁷ The photoconductor device was completed by
47
48
49
50
51 deposition of hole-selective gold contacts¹⁸ (Figure 1b,c) resulting in the formation of a
52
53
54
55
56
57
58
59
60

1
2
3 strong Schottky barrier for electrons. Our preliminary investigations focused on a P3HT:
4
5
6
7 PCBM: Bi₂O₃ weight ratio of 1:1:1 which within a photodiode architecture demonstrated
8
9
10 a sensitivity of ~1 mCmGy⁻¹cm⁻³. Initially, a photoconductor with a thickness of ~180 μm
11
12
13
14 was fabricated and the X-ray photocurrent response was tested under a 70 kVp X-ray
15
16
17 source (Figure S1) with varying X-ray dose rate (*D*) from 20 μGys⁻¹ to ~ 1 mGys⁻¹ over an
18
19
20 X-ray exposure duration of 7 s (Figure 1d) resulting in cumulative exposure doses of 0.14
21
22
23
24 - 7.5 mGy. The device demonstrated slow rise and decay behavior commensurate with
25
26
27 photo conducting characteristics. The X-ray sensitivity (*S*) was evaluated based on⁵
28
29
30

$$S = \frac{1}{D \times T_{X-ray} \times V} \int_0^{T_{X-ray}} \Delta I_{X-ray} dt \quad (1)$$

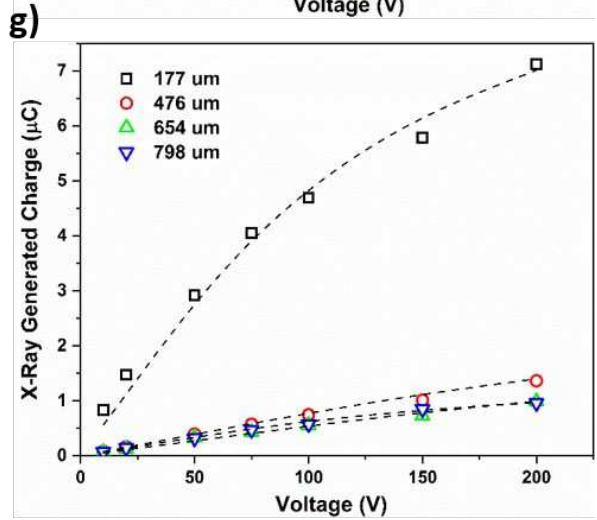
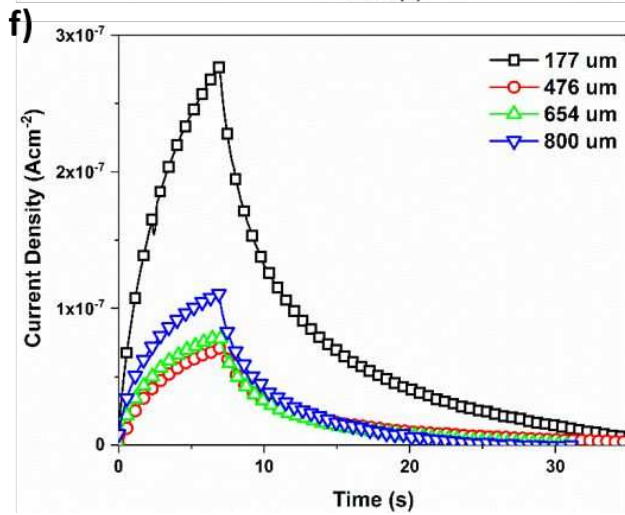
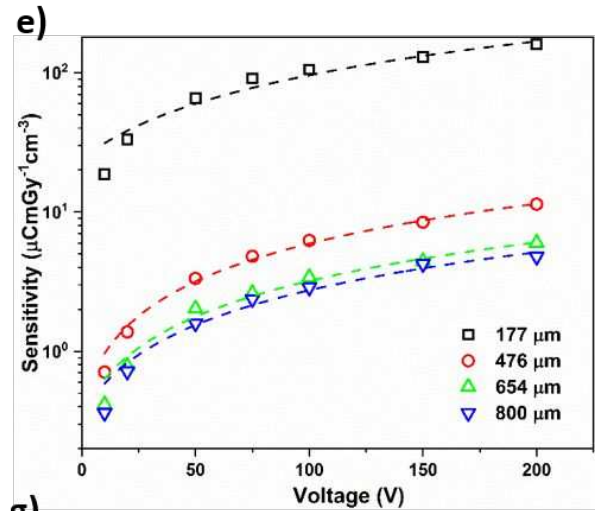
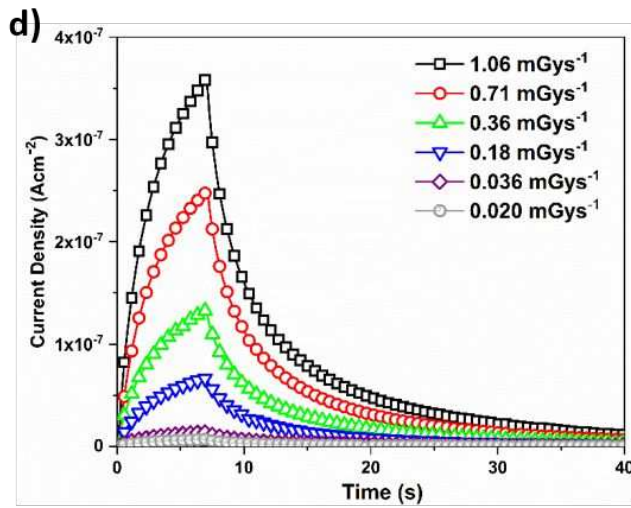
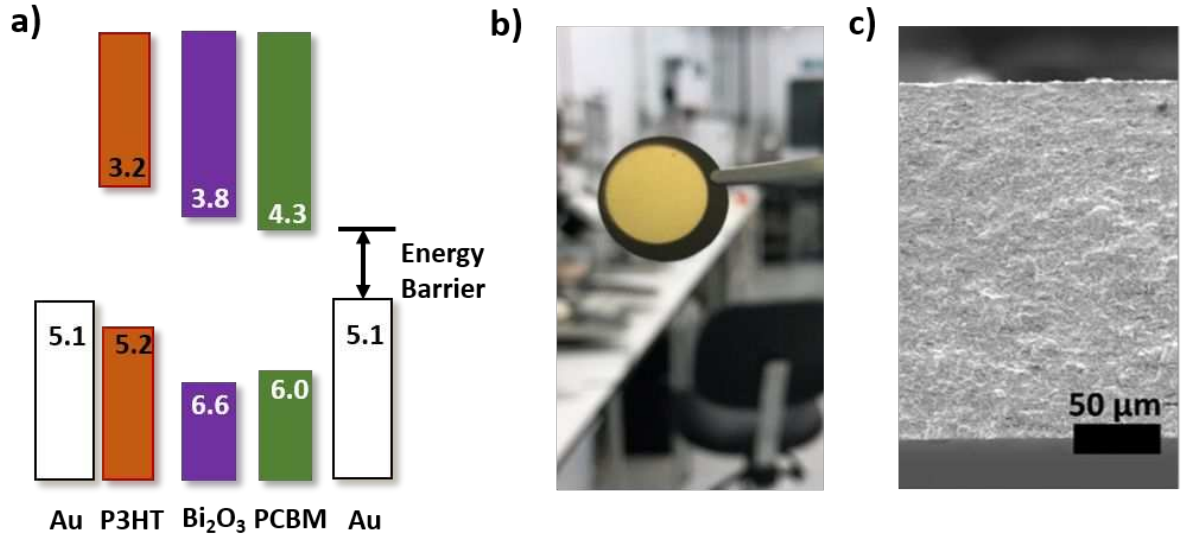
31
32
33
34
35 where ΔI_{X-ray} is the X-ray generated photocurrent over a duration of T_{X-ray} over which the
36
37
38 X-ray exposure was carried out and V is the detector volume. A high sensitivity of ~160
39
40
41 μCmGy⁻¹cm⁻³ under an applied bias of 200 V was achieved, corresponding to an electric
42
43
44 field (*E*) of ~1.2 Vμm⁻¹. These values are a significant improvement over those observed
45
46
47
48 for single crystal organic X-ray detectors¹⁹ and compete with recent reports on single
49
50
51
52
53
54
55
56
57
58
59
60

1
2
3 crystal organic and perovskite X-ray detectors (Figure S2). The mobility-time constant
4
5
6
7 ($\mu\tau$) for the above photoconductors were evaluated using the Hecht equation¹¹
8
9

$$Q = \frac{Q_0\mu\tau V}{d^2} \left[1 - \exp\left(-\frac{d^2}{\mu\tau V}\right) \right] \quad (2)$$

10
11
12
13
14 where Q is the collected charge, Q_0 is the generated charge and d is the detector
15
16
17 thickness. Fitting the above relationship to the $Q\sim V$ characteristics, a $\mu\tau$ constant of \sim
18
19
20
21 $1.7\times 10^{-6} \text{ cm}^2\text{V}^{-1}$ was obtained. This is within two orders of magnitude of the values
22
23
24 reported for printable perovskite X-ray detectors ($\mu\tau = 1 \times 10^{-4} \text{ cm}^2\text{V}^{-1}$)¹³ and chlorine
25
26
27 doped cadmium telluride single crystals ($\mu\tau = 7 \times 10^{-5} \text{ cm}^2\text{V}^{-1}$).²⁰ Based on the above $\mu\tau$
28
29
30 values, we estimate a hole drift length (L) of 170 μm . based on $L = \mu\tau E$ (for $E = 1 \text{ V}\mu\text{m}^{-1}$)
31
32
33
34
35
36
37
38
39
40
41
42
43
44
45
46
47
48
49
50
51
52
53
54
55
56
57
58
59
60
61
62
63
64
65
66
67
68
69
70
71
72
73
74
75
76
77
78
79
80
81
82
83
84
85
86
87
88
89
90
91
92
93
94
95
96
97
98
99
100
101
102
103
104
105
106
107
108
109
110
111
112
113
114
115
116
117
118
119
120
121
122
123
124
125
126
127
128
129
130
131
132
133
134
135
136
137
138
139
140
141
142
143
144
145
146
147
148
149
150
151
152
153
154
155
156
157
158
159
160
161
162
163
164
165
166
167
168
169
170
171
172
173
174
175
176
177
178
179
180
181
182
183
184
185
186
187
188
189
190
191
192
193
194
195
196
197
198
199
200
201
202
203
204
205
206
207
208
209
210
211
212
213
214
215
216
217
218
219
220
221
222
223
224
225
226
227
228
229
230
231
232
233
234
235
236
237
238
239
240
241
242
243
244
245
246
247
248
249
250
251
252
253
254
255
256
257
258
259
260
261
262
263
264
265
266
267
268
269
270
271
272
273
274
275
276
277
278
279
280
281
282
283
284
285
286
287
288
289
290
291
292
293
294
295
296
297
298
299
300
301
302
303
304
305
306
307
308
309
310
311
312
313
314
315
316
317
318
319
320
321
322
323
324
325
326
327
328
329
330
331
332
333
334
335
336
337
338
339
340
341
342
343
344
345
346
347
348
349
350
351
352
353
354
355
356
357
358
359
360
361
362
363
364
365
366
367
368
369
370
371
372
373
374
375
376
377
378
379
380
381
382
383
384
385
386
387
388
389
390
391
392
393
394
395
396
397
398
399
400
401
402
403
404
405
406
407
408
409
410
411
412
413
414
415
416
417
418
419
420
421
422
423
424
425
426
427
428
429
430
431
432
433
434
435
436
437
438
439
440
441
442
443
444
445
446
447
448
449
450
451
452
453
454
455
456
457
458
459
460
461
462
463
464
465
466
467
468
469
470
471
472
473
474
475
476
477
478
479
480
481
482
483
484
485
486
487
488
489
490
491
492
493
494
495
496
497
498
499
500
501
502
503
504
505
506
507
508
509
510
511
512
513
514
515
516
517
518
519
520
521
522
523
524
525
526
527
528
529
530
531
532
533
534
535
536
537
538
539
540
541
542
543
544
545
546
547
548
549
550
551
552
553
554
555
556
557
558
559
560
561
562
563
564
565
566
567
568
569
570
571
572
573
574
575
576
577
578
579
580
581
582
583
584
585
586
587
588
589
590
591
592
593
594
595
596
597
598
599
600
601
602
603
604
605
606
607
608
609
610
611
612
613
614
615
616
617
618
619
620
621
622
623
624
625
626
627
628
629
630
631
632
633
634
635
636
637
638
639
640
641
642
643
644
645
646
647
648
649
650
651
652
653
654
655
656
657
658
659
660
661
662
663
664
665
666
667
668
669
670
671
672
673
674
675
676
677
678
679
680
681
682
683
684
685
686
687
688
689
690
691
692
693
694
695
696
697
698
699
700
701
702
703
704
705
706
707
708
709
710
711
712
713
714
715
716
717
718
719
720
721
722
723
724
725
726
727
728
729
730
731
732
733
734
735
736
737
738
739
740
741
742
743
744
745
746
747
748
749
750
751
752
753
754
755
756
757
758
759
760
761
762
763
764
765
766
767
768
769
770
771
772
773
774
775
776
777
778
779
780
781
782
783
784
785
786
787
788
789
790
791
792
793
794
795
796
797
798
799
800
801
802
803
804
805
806
807
808
809
810
811
812
813
814
815
816
817
818
819
820
821
822
823
824
825
826
827
828
829
830
831
832
833
834
835
836
837
838
839
840
841
842
843
844
845
846
847
848
849
850
851
852
853
854
855
856
857
858
859
860
861
862
863
864
865
866
867
868
869
870
871
872
873
874
875
876
877
878
879
880
881
882
883
884
885
886
887
888
889
890
891
892
893
894
895
896
897
898
899
900
901
902
903
904
905
906
907
908
909
910
911
912
913
914
915
916
917
918
919
920
921
922
923
924
925
926
927
928
929
930
931
932
933
934
935
936
937
938
939
940
941
942
943
944
945
946
947
948
949
950
951
952
953
954
955
956
957
958
959
960
961
962
963
964
965
966
967
968
969
970
971
972
973
974
975
976
977
978
979
980
981
982
983
984
985
986
987
988
989
990
991
992
993
994
995
996
997
998
999
1000

described photoconductor. This consolidates our understanding of the improved detector
performance and rationale for their sensitivity.



1
2
3
4 **Figure 1. a) The flat band diagram for the different semiconductor materials. All energy**
5
6 **values are given in eV. b) Photograph of a fabricated X-ray detector and c) cross sectional**
7
8 **scanning electron micrograph of a detector. d) X-ray photocurrent transients under an**
9
10 **applied bias of 20 V and different dose rates over a 7 s exposure window. e) Variation in**
11
12 **the detector sensitivity under a range of applied voltages for different photoconductor**
13
14 **thicknesses, f) example transients under an electric field of 0.2 – 0.3 V μm^{-1} for different**
15
16 **photoconductor thicknesses and g) the Hecht fits for different photoconductor**
17
18 **thicknesses.**
19
20
21
22
23
24
25
26
27
28
29
30
31

32 The fraction of X-rays stopped within the active volume of the detector (F) is given
33
34
35
36 by²¹

$$F = 1 - \exp(-\mu_m \rho d) \quad (3)$$

37
38
39
40
41
42 where μ_m is the mass attenuation coefficient for a material of density ρ and thickness d .
43
44
45
46 Therefore, increasing the photoconductor thickness and/or its mass attenuation
47
48
49 coefficient enables a higher attenuation to be achieved. However, this can only be
50
51
52
53 effective if the entire detector active volume is depleted, with minimal additional
54
55
56
57
58
59
60

1
2
3 recombination centers which reduce the generated charge components. In view of the
4
5
6
7 exceptionally high carrier transport lengths observed, we first proceeded to investigate
8
9
10 the X-Ray photocurrent response of the P3HT:PCBM:Bi₂O₃ (1:1:1) system by increasing
11
12
13
14 the photoconductor thickness up to ~1 mm. Even under such high thickness, not reported
15
16
17 previously for P3HT and PCBM based organic semiconductor devices, sensitivities of ~
18
19
20 5 $\mu\text{CmGy}^{-1}\text{cm}^{-3}$ are obtained which are still competitive with the more recently reported
21
22
23
24 perovskite based X-ray detectors.¹¹ In order to ascertain the charge extraction capabilities
25
26
27 with increasing thickness, the $\mu\tau$ product was evaluated based on Hecht fits (Figure 1g)
28
29
30
31 which leads to values of $5 \times 10^{-6} \text{ cm}^2\text{V}^{-1}$ ($d = 476 \mu\text{m}$), $9 \times 10^{-6} \text{ cm}^2\text{V}^{-1}$ ($d = 654 \mu\text{m}$) and
32
33
34
35 $2.5 \times 10^{-5} \text{ cm}^2\text{V}^{-1}$ ($d = 798 \mu\text{m}$). The hole drift lengths, calculated based on the electric field
36
37
38 at $E = 1.2 \text{ V}\mu\text{m}^{-1}$, leads to an improvement in the carrier drift lengths with increasing
39
40
41
42 thickness resulting in values of ~1 mm. Such high drift lengths under low electric fields
43
44
45 are extremely beneficial in order to extract charges from detectors whose thicknesses lie
46
47
48
49 in the 100 μm – 1 mm length scale (which enables device architectures allowing a higher
50
51
52 fraction of incident X-rays to be attenuated and subsequently to be collected).
53
54
55
56
57
58
59
60

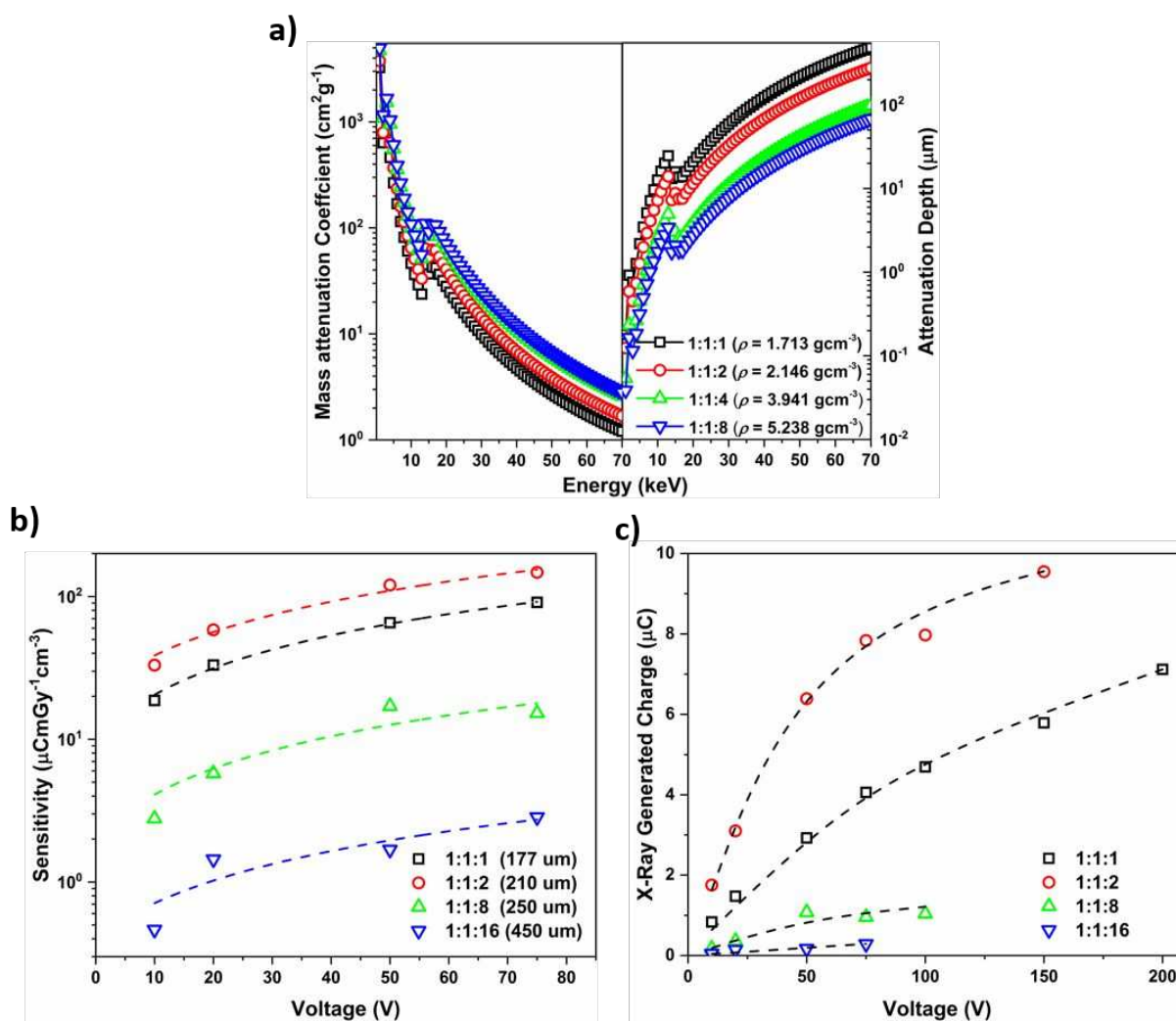
1
2
3
4 The carrier transport length scales are significantly higher than those commonly
5
6
7 employed for organic photovoltaics, where the thickness is normally restricted to < 300
8
9
10 nm,^{22,23} and for organic photodetectors,^{24,25} where the thickness is constrained to be < 1
11
12
13 μm to minimize recombination losses. On the other hand, the high drift lengths observed
14
15
16 here strongly support recent work by Gelinas *et al.*,¹⁴ where the charge separation at the
17
18 p -type organic semiconductor and n -type fullerene interface was driven through
19
20
21 delocalized states within the fullerene resulting in charge separation on a very short
22
23
24 timescale of 40 fs. While previous work has shown that photo generated electrons can be
25
26
27 transported over centimeter length scales, such large transport lengths have, so far, not
28
29
30 been utilized in an electronic device resulting in superior device performance. The ability
31
32
33 to achieve long charge transport lengths that approach millimeter length scales enables
34
35
36 the possibility to fabricate 100 μm – 1 mm thick, high sensitivity X-ray sensors based on
37
38
39 a combination of low cost organic semiconductors and high Z nanoparticles with very little
40
41
42 or no dead volume within the detector.
43
44
45
46
47
48
49
50
51
52
53
54
55

56 Impact of nanoparticle loading on X-ray photocurrent response

57
58
59
60

1
2
3
4 Following the improvement in photoconductor thickness, we then proceeded to improve
5
6
7 the X-ray stopping power by further increasing the NP loading which in turn improves μ_m .
8
9
10 This, in combination with increased detector thickness, could potentially allow for almost
11
12
13
14 100% attenuation of the incident X-ray photons thereby resulting in high sensitivities.
15
16
17 Simulation of the μ_m using NIST XCOM²⁶ (Figure 2a) for P3HT:PCBM:Bi₂O₃, where the
18
19
20 Bi₂O₃ NP loading is varied as 1:1:1, 1:1:2, 1:1:8 and 1:1:16, indicates an increase in μ_m
21
22
23
24 by $\sim \times 10$. This correspondingly reduces the X-ray attenuation length (*i.e.* the thickness
25
26
27 over which 63% of the incident X-rays are stopped) by an equivalent factor. (Figure 2a)
28
29
30
31 Under a bias voltage of – 20 V, increasing the NP loading results in a non-linear decrease
32
33
34 of the X-ray sensitivity from a high value of $\sim 40 \mu\text{CmGy}^{-1}\text{cm}^{-3}$ for 1:1:1 loading, to < 40
35
36
37 $\mu\text{CmGy}^{-1}\text{cm}^{-3}$ for higher NP loadings (Figure 2b). The reduced sensitivity despite the
38
39
40 increase in the NP loading points towards a disruption in the hole transport properties
41
42
43 within the photo conducting layer. This is indicative of a bottleneck in terms of the optimum
44
45
46 nanoparticle loading that enables sufficient attenuation of incident X-rays, together with
47
48
49 sufficient crystallinity within the charge transporting organic semiconductors to enable
50
51
52 high X-ray photocurrents to be realized. The above observations are further supported by
53
54
55
56
57
58
59
60

reduction in the $\mu\tau$ product, based on Hecht fits (Figure 2c), which decrease from 1.7×10^{-6} cm^2V^{-1} to 2×10^{-8} cm^2V^{-1} when increasing the NP loading from 1:1:1 to 1:1:16. This is suggestive of a potential limit in NP loading when designing NP sensitized organic-inorganic hybrid detectors, especially at higher thickness (>50 μm).



1
2
3
4 **Figure 2. X-ray attenuation and response characteristics under different Bi_2O_3 loadings.**

5
6
7 **a) The variation of the mass attenuation coefficient (left) and attenuation depth (right) , b)**

8
9
10 **X-ray sensitivity and c) X-ray generated charges under applied bias with Hecht fits for**

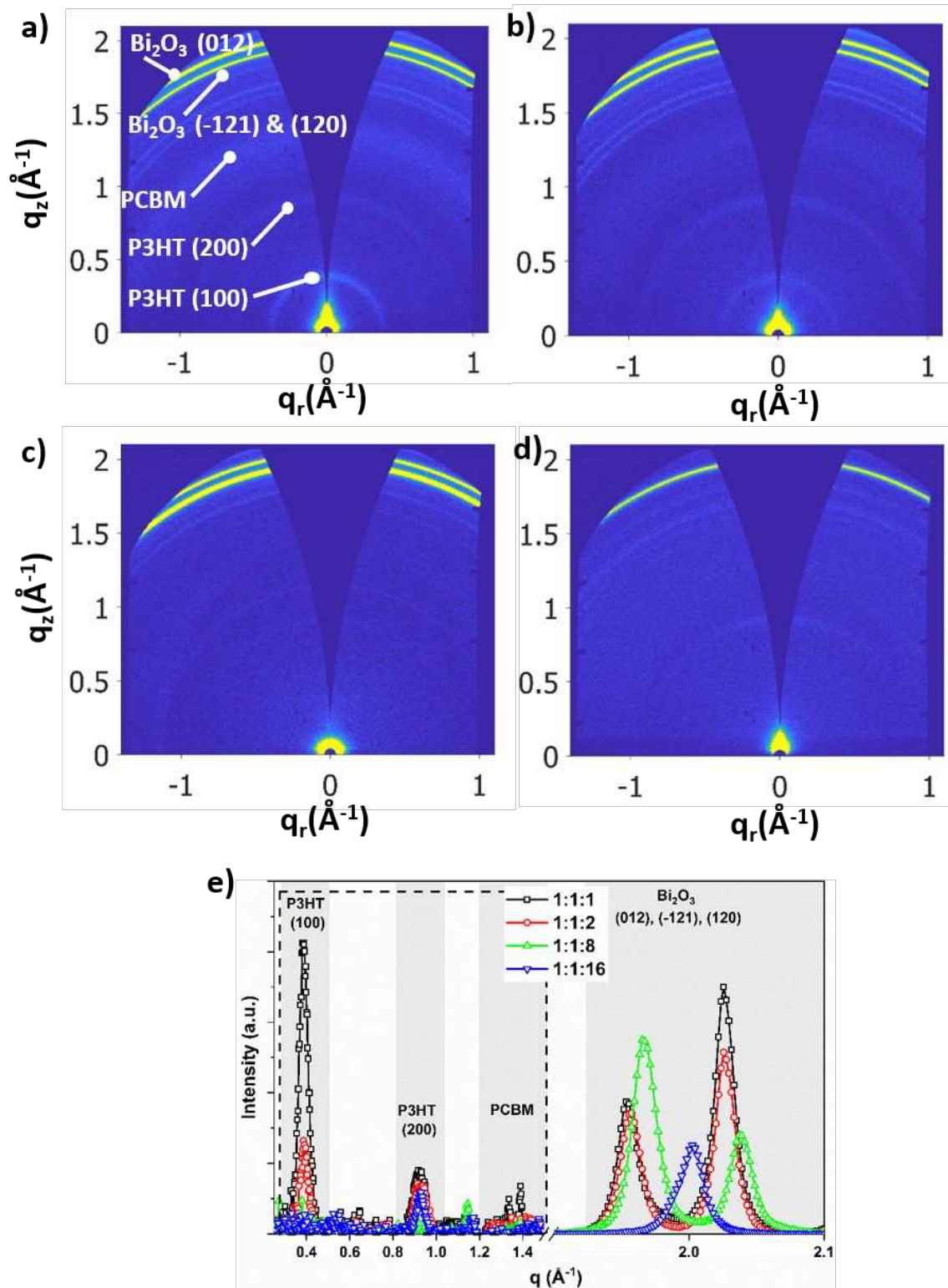
11
12
13 **P3HT:PCBM: Bi_2O_3 photoconductors for 1:1:1, 1:1:2, 1:1:8 and 1:1:16 ratios.**

14 15 16 17 18 **Impact of nanoparticle loading on the organic semiconductor crystallinity**

19
20
21
22
23 One of the dominant structural properties that affect the performance of such detectors
24
25
26 is the crystallinity of the organic semiconductor systems used. In the case of the detector
27
28
29 architecture utilized in this work, achieving a high crystallinity for the P3HT phase is
30
31
32 preferable as this would have direct impact on the charge transport properties.⁵ In order
33
34
35 to observe the impact of the NP loading on the crystallinity of the P3HT, we carried out
36
37
38 grazing incidence wide angle x-ray scattering (GIWAXS) measurements on pressed
39
40
41 pellets (Figure 3a) and analyzed the evolution of the X-ray scattering peaks for the P3HT,
42
43
44 PCBM and Bi_2O_3 NP phases (Figure 3a). Based on the X-ray scattering spectra, it is
45
46
47 evident that increasing the P3HT:PCBM: Bi_2O_3 ratio from 1:1:1 to 1:1:2 results in a
48
49
50 decrease in intensity for the scattering peaks related to the P3HT phase ((100) and (200))
51
52
53
54
55
56
57
58
59
60

1
2
3 planes))⁵ while these peaks are not observed for the higher NP loadings of 1:1:8 and
4
5
6
7 1:1:16. The higher intensities observed for the (100) plane of P3HT indicates that despite
8
9
10 the powder nature of the starting material, P3HT has a more preferential “edge on”
11
12
13 orientation where the P3HT lamellar align parallel to the planar surface of the pellet with
14
15
16 the side chains oriented perpendicular to the planar pellet surface. With regards to the
17
18
19
20
21 PCBM, we note that a noticeable scattering peak is unobservable. This is attributed to the
22
23
24 GIWAXS spectra being strongly dominated by the scatter peaks due to the Bi₂O₃ NPs
25
26
27 resulting in weakly scattering peaks (such as those due to the PCBM phase) to be
28
29
30
31 unobservable. The observation of sharp peaks in the GIWAXS spectra for the Bi₂O₃ NPs
32
33
34 are in agreement with the crystalline nature of this material whose characteristics based
35
36
37 on X-ray powder diffraction studies were reported previously.⁵ In order to verify that the
38
39
40
41 loss of crystallinity is not due to the fabrication methodology utilized, we carried out
42
43
44
45 differential scanning calorimetry (DSC) on the P3HT:PCBM:Bi₂O₃ starting powders used
46
47
48
49 for the fabrication of the pellets (Figure S3).²⁰ DSC analysis for the P3HT phase in
50
51
52 P3HT:PCBM:Bi₂O₃ samples at ratios of 1:1:1 and 1:1:2 shows crystallinity of around 5-
53
54
55
56 6%. On the other hand, the crystallinity of P3HT is well below the limits that can be
57
58
59
60

1
2
3 observed for the 1:1:8 and 1:1:16 systems which is in agreement with the observations
4
5
6
7 made from the GIWAXS analysis. The loss in crystallinity for the P3HT phase which in
8
9
10 the detector architecture utilized here explains the poor sensitivity and $\mu\tau$ constants for
11
12
13 the 1:1:8 and 1:1:16 samples where the charge extraction is inhibited due to the more
14
15
16
17 disordered nature of the hole transporting P3HT phase.
18
19
20
21
22
23
24
25
26
27
28
29
30
31
32
33
34
35
36
37
38
39
40
41
42
43
44
45
46
47
48
49
50
51
52
53
54
55
56
57
58
59
60



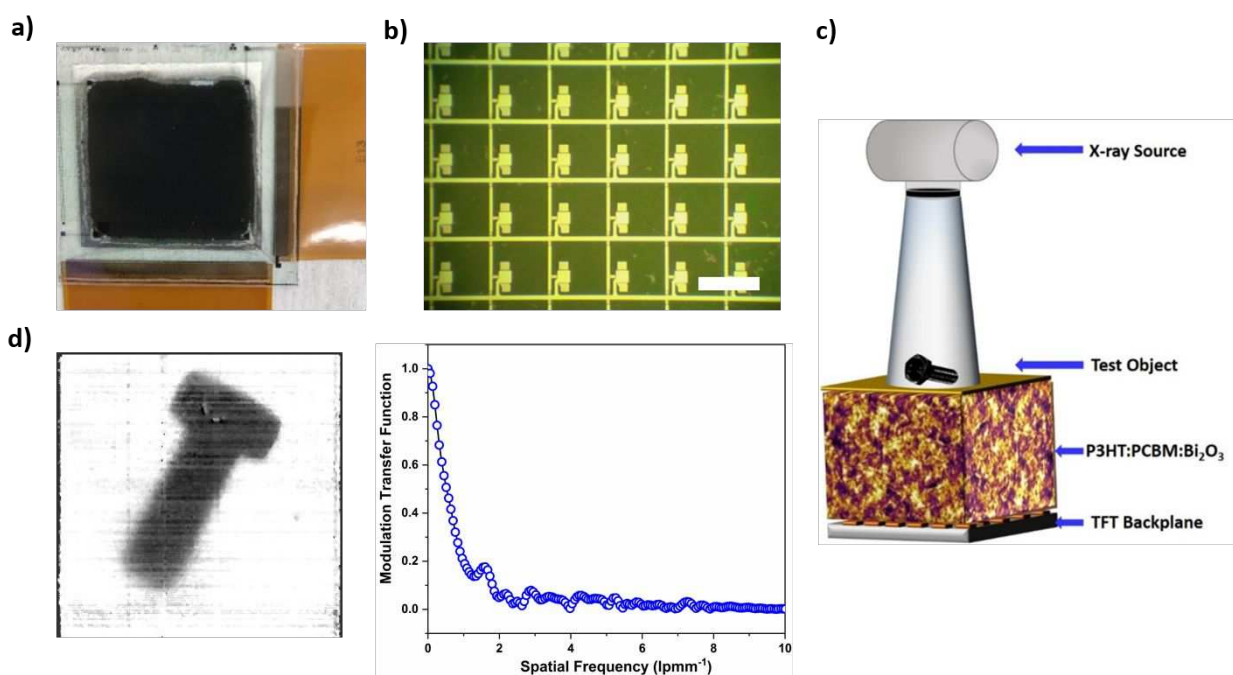
1
2
3
4 Figure 3. 2D GIWAXS spectra for the hybrid pellets based on P3HT:PCBM:Bi₂O₃ NP
5
6
7 ratios of a) 1:1:1, b) 1:1:2, c) 1:1:8 and d) 1:1:16. e) 1D spectra extracted from the 2D
8
9
10 GIWAXS plots. A noticeable decrease in the peak intensities for the (100) and (200) P3HT
11
12
13 crystalline planes are observed for 1:1:8 and 1:1:16 samples indicating loss of P3HT
14
15
16 crystallinity while scatter peaks for the PCBM phase are not observable due to the high
17
18
19 scattering intensities of the Bi₂O₃ NPs. The X-ray scattering intensities in the range of q
20
21 = 0.2 – 1.5 Å⁻¹ (indicated by the dashed box) have been scaled by x30.
22
23
24
25
26
27
28
29
30

31 X-ray imaging characteristics

32
33
34

35 Finally, we proceeded to fabricate an X-ray imager (Figure 4a) based on the best
36
37 performing P3HT:PCBM:Bi₂O₃ 1:1:1 loading condition at a detector thickness of ~250 μm.
38
39
40 For the fabrication of an array of detector pixels, for imaging purposes, the photo
41
42 conducting wafer was interfaced by contacting an array of thin film transistors (Figure 4b),
43
44
45
46 The spatial resolution of the detector was determined using the modulation transfer
47
48
49 function (MTF) (Figure 4e) *via* the slanted edge method. The MTF of the
50
51
52
53
54
55
56
57
58
59
60

1
2
3 P3HT:PCBM:Bi₂O₃ based imager possesses a value of 0.2 at ~1 lpmm⁻¹ which is suitable
4
5
6
7 for applications where millimeter to submillimeter scale features require to be
8
9
10 discriminated as in for example, baggage scanning in border security. Therefore, we
11
12
13 envisage these photoconductors to be used for X-ray imaging in security applications
14
15
16
17 where the feature sizes of the objects observed are larger than several millimeters.
18
19
20



44 Figure 4. X-ray imager characteristics. a) photograph of the 1st generation imager
45 prepared using a ratio of 1:1:1 P3HT:PCBM:Bi₂O₃, and detector thickness of 250 μm. b)
46
47 photograph of pixelated array where each pixel is addressed by a transistor (scale bar =
48
49
50
51
52
53
54
55
56
57
58
59
60 100 μm). c) schematic of the imager architecture where the individual pixels are

1
2
3 addressed using a matrix of transistors as shown in b). d) X-ray image of a screw obtained
4
5
6
7 using the imager and e) the MTF of the imager as obtained based on the slanted edge
8
9
10 method.

11 12 13 14 15 **Avenues for future developments**

16
17
18
19 While the detector architecture developed in this work shows promise for dosimetry and
20
21
22 imaging applications, further developments of several key parameters are required in
23
24
25
26 order for this architecture to be truly competitive with existing commercial technologies.
27
28
29 The rise and decay times of the devices presented here (as evident in the transient X-ray
30
31
32 photocurrent responses given in Figures 1d,f) proceeds over several seconds. This is in
33
34
35
36 contrast to commercial detector materials such as those based on the combination of
37
38
39 cesium iodide scintillators and amorphous silicon photodiodes which have been optimized
40
41
42 to obtain > 10 frames per second,²⁷ diamond single crystals²⁸ (rise and fall times of ~1.1
43
44
45 s and ~0.4 s, the latter limited by measurement apparatus used) as well as cadmium zinc
46
47
48 telluride single crystals (rise and fall times < 100 ns).²⁹ As the rise and decay times are
49
50
51
52
53
54 often a reflection of the charge trapping and de-trapping processes taking place within
55
56
57
58
59
60

1
2
3 the relatively disordered organic semiconductor matrix (in comparison to its inorganic
4
5
6
7 counterparts), we speculate that the replacement of the current organic semiconductors
8
9
10 or inclusion of a inorganic material possessing higher carrier mobilities are likely to lead
11
12
13 to significant improvement in the response times. Potential solution processible high
14
15
16 mobility semiconductors includes organic semiconductors developed for organic thin film
17
18 transistor applications such as 6,13-bis(triisopropylsilylethynyl)³⁰ or poly[4-(4,4-
19
20 dihexadecyl-4H-cyclopenta[1,2-b:5,4-b']dithiophen-2-yl)-alt-[1,2,5]-thiadiazolo[3,4-
21
22 c]pyridine].³¹
23
24
25
26
27
28
29
30

31 The second key factor that affects the performance of the detector architecture
32
33 developed for both dosimetry and imaging is the high pixel dark currents observed (Figure
34
35 S4) which leads to a signal to noise ratio < 0.2. This in turn results in images that display
36
37
38 very low contrast (as visually evident from Figure 4d) as well as limit the dynamic range
39
40
41 of the detector. Among organic semiconductors used for organic photodiode applications
42
43
44 (including for indirect radiation detection), P3HT has been observed to result in high dark
45
46
47 currents.⁶ On the other hand, *p*-type organic semiconductors such as poly[N-9'-
48
49 heptadecanyl-2,7-carbazole-alt-5,5-(4',7'-di-2-thienyl-2',1',3'-benzothiadiazole)] as well
50
51
52
53
54
55
56
57
58
59
60

1
2
3 as several other non-disclosed polymers have been reported to result in dark currents <
4
5
6
7 1 nAcm^{-2} ^{32,33} approaching the performance of amorphous silicon photodiodes.
8
9

10 Replacement of the current P3HT system with the above p -type semiconductors is more
11
12
13
14 than likely to enable the detector dark current to be reduced to an industry acceptable
15
16
17 level of 0.1 nAcm^{-2} .
18
19

20 21 CONCLUSION

22
23
24
25 In conclusion, we have demonstrated hole drift lengths in P3HT:PCBM:Bi₂O₃
26
27
28 heterojunction architectures exceeding 100 μm , where the PCBM phase acts as an
29
30
31
32 electron trap enabling hole only device behavior. The high hole transport lengths enable
33
34
35 thick P3HT:PCBM:Bi₂O₃ device fabrication for high X-ray attenuation resulting in a best
36
37
38 X-ray sensitivity of $\sim 160 \mu\text{CmGy}^{-1}\text{cm}^{-3}$. Based on the above, the possibility of increasing
39
40
41
42 the X-ray attenuation through increased nanoparticle loading was investigated. However,
43
44
45 a noticeable decrease in the X-ray sensitivity was observed. Structural studies carried out
46
47
48
49 based on varying nanoparticle loading suggests that the increased nanoparticle length
50
51
52
53 leads to a loss in P3HT crystallinity which results in the degradation of the X-ray
54
55
56
57
58
59
60

1
2
3 photocurrent response, hence indicating the importance of an optimized nanoparticle
4
5
6 loading for such hybrid “inorganics-in-organics” materials. Based on the above
7
8
9 observations, a prototype imager was developed combining the P3HT:PCBM:Bi₂O₃ X-ray
10
11
12 photoconductor with an a-Si backplane. The resulting imager demonstrates an MTF value
13
14
15 of $\sim 1 \text{ lpmm}^{-1}$ which indicates the possibility of resolving features in the millimeter length
16
17
18 scales with potential applications such as in dose mapping for radiotherapy, scanning at
19
20
21 border control. However, there still exists several key characteristics features such as the
22
23
24 reduction of dark current, improving rise and decay times that would enable systems to
25
26
27 be utilized for dynamic X-ray imaging. Such developments are expected through
28
29
30 developments in organic semiconductors with high mobilities, which in combination with
31
32
33 the characteristics developed here are expected to enable a broad range of applications.
34
35
36
37
38
39
40
41
42
43
44
45
46
47
48
49

50 MATERIALS AND METHODS

51
52
53
54
55
56
57
58
59
60

1
2
3
4 **Powder preparation.** Regioregular P3HT (Rieke) and PCBM (Solenne) were added to
5
6
7 anhydrous chloroform at concentrations of 80 mgml⁻¹ each and left to stir overnight. Bi₂O₃
8
9
10 nanopowder with an average particle size of 38 nm was added to form P3HT:PCBM:Bi₂O₃
11
12
13 mixtures with weight loadings as described. The mixture was left to stir overnight. Addition
14
15
16 of the organic semiconductors and the Bi₂O₃ nanopowder was carried out in a N₂ glove
17
18
19 box (MBraun) with O₂ and H₂O content of < 1 ppm. For precipitation of the powders, 1 ml
20
21
22 of ethanol was added to 1 ml of the starting solution and then rotary evaporated. The
23
24
25 dried powder was then further dried under vacuum overnight to remove any residual
26
27
28 solvent.
29
30
31
32
33
34

35 **Wafer and detector preparation.** A hydraulic press (Perkin Elmer FTIR pellet press) with
36
37
38 a 15 mm die was used for sintering. A polished stainless-steel cylinder was placed in the
39
40
41 bore of the cylinder body by an Al foil. 100–1000 mg of the P3HT:PCBM:Bi₂O₃ powder
42
43
44 was then loaded into the bore. Next, a second polished cylinder which is covered by an
45
46
47 Al foil and a plunger were inserted into the cylinder body. A 1000 kg load was applied to
48
49
50 form the pellet for 15 min with the pellet pressing being carried out at room temperature.
51
52
53
54
55
56
57
58
59
60

1
2
3
4 The use of the Al foils enables a visual identification of the smoothness of the pressed
5
6
7 pellets. For completion of the photoconductor devices, 100 nm of gold with an overlap
8
9
10 area of 1 cm² was sputtered through a shadow mask.

11
12
13
14 **X-ray photocurrent response measurement.** The X-ray photo response was obtained
15
16
17 using a 70 kV X-ray source (Siemens MEGALIX Cat Plus 125/40/90, 124 GW) with a
18
19 tungsten anode. The X-ray spectrum was filtered with a 2.5-mm-thick Al plate. The dose
20
21
22 rate was varied by changing the X-ray tube current with calibrated with a PTW Diados
23
24
25 T11003-001896 dosimeter. Electrical readouts were carried out using a Keithley 2400
26
27
28 source measure unit at 100 ms. Image read-out and processing: A 256 × 256 amorphous
29
30
31 silicon thin film transistor panel was used for the imager in conjunction with a commercially
32
33
34 available read-out IC (ROIC) (ISC9717 from Flir). The pixel pitch is 98 μm. The input
35
36
37 signal was integrated, amplified and subjected to a low pass filter simultaneously and
38
39
40 converted from analog to digital using a 14-bit AD converter. The integrator feedback
41
42
43 capacitance used was 2 pF and the integration time was 10 ms. Dark images taken with
44
45
46 and without the sensor, were used in order to evaluate the noise of the system. Dark
47
48
49
50
51
52
53
54
55
56
57
58
59
60

1
2
3
4 image and flat field correction was carried out to obtain X-ray recordings. The modulation
5
6
7 transfer function (MTF) was determined using the slanted-edge method³⁴ *via* an ImageJ
8
9
10 plug-in.

11
12
13
14 **GIWAXS.** GIWAXS measurements were performed using a Xeuss 2.0 (XENOCSS,
15
16
17 France) system equipped with a MetalJet (Excillum, Sweden) liquid gallium source which
18
19
20 provides a 9.24 keV X-ray beam. The beam was collimated to a spot of with a lateral
21
22
23 dimension of 400 μm on the sample. Pilatus3R 1M 2D detector (Dectris, Switzerland)
24
25
26 placed at ~ 311 mm from the sample was used to obtain the diffraction images. Calibration
27
28
29 of the sample=detector distance was carried out using a silver behenate calibrant in
30
31
32 transmission geometry while the GIWAXS measurements were carried out at an incident
33
34
35 angle of 0.3° . The diffraction images were then remapped from pixel to scattering vector
36
37
38
39 using the software Foxtrot (Soleil France).
40
41
42
43
44
45

46 47 **ASSOCIATED CONTENT** 48 49 50 51 52 53 54 55 56 57 58 59 60

1
2
3 K.D.G.I.J., H.M.T., C.A.M. & S.R.P.S. have a filed patent (Direct Conversion Radiation
4
5
6
7 Detector, International Publication Number: WO 2018/078372 A1) which is assigned to a
8
9
10 startup company (SilverRay Ltd.).
11
12
13
14
15
16
17

18 **Supporting Information.**

19
20
21 The Supporting Information is available free of charge on the ACS Publications website
22
23
24 at **XXX**
25
26
27

28
29 The Supporting Information provided consists of additional details regarding the simulated
30
31
32 X-ray photon density spectrum, X-ray sensitivity comparison chart, DSC analysis and
33
34
35
36 dark current characteristics.
37
38
39
40
41
42

43 **AUTHOR INFORMATION**

44 45 46 **Author Contributions**

47
48
49
50
51 K.D.G.I.J. and H.M.T. conceived the idea and planned the project with additional input
52
53
54 from S.F.T and C.A.M; prepared the powder for the fabrication of pellets. J.E.H. fabricated
55
56
57
58
59
60

1
2
3 the pellets and the imager while H.M.T. and S.F.T. carried out the X-ray detector and
4
5
6 imager characterization. K.D.G.I.J. analyzed the X-ray photoconductor data while S.F.T.
7
8
9
10 analyzed the measurements from the X-ray imager. A.J.P. carried out the GIWAXS
11
12
13 measurements and analyzed the data with contribution from K.D.G.I.J. R.M.I.B. prepared
14
15
16 samples for SEM measurements, and for DSC characterization and analyzed the results
17
18
19 obtained. C.A.M and S.R.P.S. proposed the project and oversaw the delivery of the
20
21
22 project objectives. K.D.G.I.J. drafted the manuscript and compiled the figures. All authors
23
24
25
26
27 discussed the results and provided feedback on the manuscript.
28
29
30
31
32
33
34

35 **ACKNOWLEDGMENT**

36
37
38
39
40 K.D.G.I.J., H.M.T., C.A.M. and S.R.P.S. gratefully acknowledge support for this work
41
42
43 from the Leverhulme Trust through research project grant (RPG-2014-312). S.R.P.S.
44
45
46 acknowledges EPSRC for funding through research project grant (EP/R025304/1).
47
48
49
50 R.M.I.B. acknowledges support from the University of Surrey Overseas Research
51
52
53
54 Scholarship/University Research Scholarship. The GIWAXS measurements were
55
56
57
58
59
60

1
2
3 performed on the Sheffield Xeuss 2.0 SAXS instrument, A.J.P. is grateful to Xenocs for
4
5
6
7 their ongoing help and support in the user program at the University of Sheffield. We
8
9
10 thank V. Doukova (University of Surrey) for providing assistance on obtaining DSC
11
12
13
14 results.
15
16
17

18 References

- 19
20
21 (1) Meng, L.; Zhang, Y.; Wan, X.; Li, C.; Zhang, X.; Wang, Y.; Ke, X.; Xiao, Z.; Ding,
22 L.; Xia, R.; Yip, H.-L.; Cao, Y.; Chen, Y. Organic And Solution-Processed Tandem Solar
23 Cells With 17.3% Efficiency. *Science* **2018**, 361, 1094–1098.
24
25
26
27 (2) Che, X.; Li, Y.; Qu, Y.; Forrest, S. R. High Fabrication Yield Organic Tandem
28 Photovoltaics Combining Vacuum- And Solution-Processed Subcells With 15% Efficiency.
29 *Nat. Energy* **2018**, 3, 422–427.
30
31
32
33 (3) Jayawardena, K. D. G. I.; Rozanski, L. J.; Mills, C. A.; Beliatas, M. J.; Nismy, N. A.;
34 Silva, S. R. P. ‘Inorganics-In-Organics’: Recent Developments And Outlook For 4G
35 Polymer Solar Cells. *Nanoscale* **2013**, 5, 8411–8427.
36
37
38
39 (4) Liu, Y.; Li, C.; Ren, Z.; Yan, S.; Bryce, M. R. All-Organic Thermally Activated Delayed
40 Fluorescence Materials For Organic Light-Emitting Diodes. *Nat. Rev. Mater.* **2018**, 3,
41 18020.
42
43
44
45 (5) Thirimanne, H. M.; Jayawardena, K. D. G. I.; Parnell, A. J.; Bandara, R. M. I.;
46 Karalasingam, A.; Pani, S.; Huerdler, J. E.; Lidzey, D. G.; Tedde, S. F.; Nisbet, A.;
47 Mills, C. A.; Silva, S. R. P. High Sensitivity Organic Inorganic Hybrid X-Ray Detectors
48 With Direct Transduction And Broadband Response. *Nat. Commun.* **2018**, 9, 2926.
49
50
51
52
53
54
55
56
57
58
59
60

- 1
2
3
4 (6) Büchele, P.; Richter, M.; Tedde, S. F.; Matt, G. J.; Anka, G. N.; Fischer, R.; Biele,
5 M.; Metzger, W.; Lilliu, S.; Bikondoa, O.; Macdonald, J. E.; Brabec, C. J.; Kraus, T.;
6 Lemmer, U.; Schmidt, O. X-Ray Imaging With Scintillator-Sensitized Hybrid Organic
7 Photodetectors. *Nat. Photonics* **2015**, *9*, 843–848.
8
9
10
11 (7) Intaniwet, A.; Mills, C. A.; Shkunov, M.; Sellin, P. J.; Keddie, J. L. Heavy Metallic
12 Oxide Nanoparticles For Enhanced Sensitivity In Semiconducting Polymer X-Ray
13 Detectors. *Nanotechnology* **2012**, *23*, 235502.
14
15
16
17 (8) Mills, C. A.; Al-Otaibi, H.; Intaniwet, A.; Shkunov, M.; Pani, S.; Keddie, J. L.; Sellin,
18 P. J. Enhanced X-Ray Detection Sensitivity In Semiconducting Polymer Diodes
19 Containing Metallic Nanoparticles. *J. Phys. D. Appl. Phys.* **2013**, *46*, 275102.
20
21
22
23 (9) Ciavatti, A.; Basiricò, L.; Fratelli, I.; Lai, S.; Cosseddu, P.; Bonfiglio, A.; Anthony, J.
24 E.; Fraboni, B. Boosting Direct X-Ray Detection In Organic Thin Films By Small
25 Molecules Tailoring. *Adv. Funct. Mater.* **2018**, *29*, 1806119.
26
27
28
29
30 (10) Basiricò, L.; Ciavatti, A.; Cramer, T.; Cosseddu, P.; Bonfiglio, A.; Fraboni, B. Direct
31 X-Ray Photoconversion In Flexible Organic Thin Film Devices Operated Below 1 V. *Nat.*
32 *Commun.* **2016**, *7*, 13063.
33
34
35
36 (11) Shrestha, S.; Fischer, R.; Matt, G. J.; Feldner, P.; Michel, T.; Osvet, A.; Levchuk,
37 I.; Merle, B.; Golkar, S.; Chen, H.; Tedde, S. F.; Schmidt, O.; Hock, R.; Rührig, M.;
38 Göken, M.; Heiss, W.; Anton, G.; Brabec, C. J. High-Performance Direct Conversion
39 X-Ray Detectors Based On Sintered Hybrid Lead Triiodide Perovskite Wafers. *Nat.*
40 *Photonics* **2017**, *11*, 436–440.
41
42
43
44
45 (12) He, Y.; Matei, L.; Jung, H. J.; McCall, K. M.; Chen, M.; Stoumpos, C. C.; Liu, Z.;
46 Peters, J. A.; Chung, D. Y.; Wessels, B. W.; Wasielewski, M. R.; Dravid, V. P.;
47 Burger, A.; Kanatzidis, M. G. High Spectral Resolution Of Gamma-Rays At Room
48 Temperature By Perovskite CsPbBr₃ Single Crystals. *Nat. Commun.* **2018**, *9*, 1609.
49
50
51
52
53
54
55
56
57
58
59
60

- 1
2
3
4 (13) Kim, Y. C.; Kim, K. H.; Son, D.-Y.; Jeong, D.-N.; Seo, J.-Y.; Choi, Y. S.; Han, I. T.;
5 Lee, S. Y.; Park, N.-G. Printable Organometallic Perovskite Enables Large-Area, Low-
6 Dose X-Ray Imaging. *Nature* **2017**, *550*, 87–91.
7
8
9
10 (14) Gélinas, S.; Rao, A.; Kumar, A.; Smith, S. L.; Chin, A. W.; Clark, J.; van der Poll, T.
11 S.; Bazan, G. C.; Friend, R. H. Ultrafast Long-Range Charge Separation In Organic
12 Semiconductor Photovoltaic Diodes. *Science* **2014**, *343*, 512–516.
13
14
15
16 (15) Burlingame, Q.; Coburn, C.; Che, X.; Panda, A.; Qu, Y.; Forrest, S. R. Centimetre-
17 Scale Electron Diffusion In Photoactive Organic Heterostructures. *Nature* **2018**, *554*, 77–
18 80.
19
20
21
22 (16) Ciavatti, A.; Capria, E.; Fraleoni-Morgera, A.; Tromba, G.; Dreossi, D.; Sellin, P. J.;
23 Cosseddu, P.; Bonfiglio, A.; Fraboni, B. Toward Low-Voltage And Bendable X-Ray
24 Direct Detectors Based On Organic Semiconducting Single Crystals. *Adv. Mater.* **2015**,
25 *27*, 7213–7220.
26
27
28
29
30 (17) Armin, A.; Shoaee, S.; Lin, Q.; Burn, P. L.; Meredith, P. On The Unipolarity Of Charge
31 Transport In Methanofullerene Diodes. *npj Flex. Electron.* **2017**, *1*, 13.
32
33
34
35 (18) Dabera, G. D. M. R.; Jayawardena, K. D. G. I.; Prabhath, M. R. R.; Yahya, I.; Tan,
36 Y. Y.; Nismy, N. A.; Shiozawa, H.; Sauer, M.; Ruiz-Soria, G.; Ayala, P.; Stolojan,
37 V.; Adikaari, A. A. D. T.; Jarowski, P. D.; Pichler, T.; Silva, S. R. P. Hybrid Carbon
38 Nanotube Networks As Efficient Hole Extraction Layers For Organic Photovoltaics. *ACS*
39 *Nano* **2013**, *7*, 556–565.
40
41
42
43
44 (19) Fraboni, B.; Fraleoni-Morgera, A.; Zaitseva, N. Ionizing Radiation Detectors Based On
45 Solution-Grown Organic Single Crystals. *Adv. Funct. Mater.* **2016**, *26*, 2276–2291.
46
47
48
49 (20) Sellin, P. J.; Davies, A. W.; Lohstroh, A.; Ozsan, M. E.; Parkin, Drift Mobility And
50 Mobility-Lifetime Products In Cdte:Cl Grown By The Travelling Heater Method. *J. IEEE*
51 *Trans. Nucl. Sci.* **2005**, *52*, 3074–3078.
52
53
54
55
56
57
58
59
60

- 1
2
3
4 (21) X-Ray Mass Attenuation Coefficients | NIST <https://www.nist.gov/pml/x-ray-mass-attenuation-coefficients> (accessed Oct 5, 2018).
5
6
7
- 8 (22) Park, S. H.; Roy, A.; Beaupré, S.; Cho, S.; Coates, N.; Moon, J. S.; Moses, D.;
9 Leclerc, M.; Lee, K.; Heeger, A. J. Bulk Heterojunction Solar Cells With Internal
10 Quantum Efficiency Approaching 100%. *Nat. Photonics* **2009**, *3*, 297–302.
11
12
13
- 14 (23) He, Z.; Xiao, B.; Liu, F.; Wu, H.; Yang, Y.; Xiao, S.; Wang, C.; Russell, T. P.; Cao,
15 Y. Single-Junction Polymer Solar Cells With High Efficiency And Photovoltage. *Nat.*
16 *Photonics* **2015**, *9*, 174–179.
17
18
19
- 20 (24) Armin, A.; Hamsch, M.; Kim, I. K.; Burn, P. L.; Meredith, P.; Namdas, E. B. Thick
21 Junction Broadband Organic Photodiodes. *Laser Photon. Rev.* **2014**, *8*, 924–932.
22
23
24
- 25 (25) Armin, A.; Jansen-van Vuuren, R. D.; Kopidakis, N.; Burn, P. L.; Meredith, P.
26 Narrowband Light Detection *Via* Internal Quantum Efficiency Manipulation Of Organic
27 Photodiodes. *Nat. Commun.* **2015**, *6*, 6343.
28
29
30
- 31 (26) US Department Of Commerce, NIST XCOM: Photon Cross Sections Database,
32 <http://www.nist.gov/pml/data/xcom/>, accessed: December, 2018.
33
34
- 35 (27) Medical Flat Panel Detectors | Varex Imaging
36 <https://www.vareximaging.com/products/medical/medical-flat-panel-detectors>
37 (accessed Apr 8, 2019).
38
39
40
- 41 (28) Abdel-Rahman, M. A. E.; Lohstroh, A.; Jayawardena, I.; Henley, S. J. The X-Ray
42 Detection Performance Of Polycrystalline CVD Diamond With Pulsed Laser
43 Deposited Carbon Electrodes. *Diam. Relat. Mater.* **2012**, *22*, 70–76.
44
45
46
47
- 48 (29) Zhao, X. C.; Ouyang, X. P.; Xu, Y. D.; Han, H. T.; Zhang, Z. C.; Wang, T.; Zha, G.
49 Q.; Ouyang, X. Time Response Of Cd_{0.9}Zn_{0.1}Te Crystals Under Transient And
50 Pulsed Irradiation. *AIP Adv.* **2012**, *2*, 012162.
51
52
53
54
55
56
57
58
59
60

- 1
2
3
4 (30) Intaniwet, A.; Keddie, J. L.; Shkunov, M.; Sellin, P. J. High Charge-Carrier Mobilities
5 In Blends Of Poly(Triarylamine) And TIPS-Pentacene Leading To Better
6 Performing X-Ray Sensors. *Org. Electron.* **2011**, *12*, 1903–1908.
7
8
9
10 (31) Luo, C.; Kyaw, A. K. K.; Perez, L. A.; Patel, S.; Wang, M.; Grimm, B.; Bazan, G. C.;
11 Kramer, E. J.; Heeger, A. J. General Strategy For Self-Assembly Of Highly Oriented
12 Nanocrystalline Semiconducting Polymers With High Mobility. *Nano Lett.* **2014**, *14*,
13 2764–2771.
14
15
16
17
18 (32) Kielar, M.; Dhez, O.; Pecastaings, G.; Curutchet, A.; Hirsch, L. Long-Term Stable
19 Organic Photodetectors With Ultra Low Dark Currents For High Detectivity
20 Applications. *Sci. Rep.* **2016**, *6*, 39201.
21
22
23
24 (33) Gelinck, G. H.; Kumar, A.; Moet, D.; van der Steen, J.-L. P. J.; van Breemen, A. J.
25 J. M.; Shanmugam, S.; Langen, A.; Gilot, J.; Groen, P.; Andriessen, R.; Simon, M.;
26 Ruetten, W.; Douglas, A. U.; Raaijmakers, R.; Malinowski, P. E.; Myny, K. X-Ray
27 Detector-On-Plastic With High Sensitivity Using Low Cost, Solution-Processed
28 Organic Photodiodes. *IEEE Trans. Electron Devices* **2016**, *63*, 197–204.
29
30
31
32
33
34 (34) Samei, E.; Flynn, M. J.; Reimann, D. A. A Method For Measuring The Presampled
35 MTF Of Digital Radiographic Systems Using An Edge Test Device. *Med. Phys.*
36 **1998**, *25*, 102–113.
37
38
39
40 (35) Yakunin, S.; Dirin, D. N.; Shynkarenko, Y.; Morad, V.; Cherniukh, I.; Nazarenko, O.;
41 Kreil, D.; Nauser, T.; Kovalenko, M. V. Detection Of Gamma Photons Using Solution-
42 Grown Single Crystals Of Hybrid Lead Halide Perovskites. *Nat. Photonics* **2016**, *10*,
43 585–589.
44
45
46
47
48 (36) Mills, C. A.; Intaniwet, A.; Shkunov, M.; Keddie, J. L.; Sellin, P. J. Flexible Radiation
49 Dosimeters Incorporating Semiconducting Polymer Thick Films. *Proc. SPIE*, **2009**, 7449,
50 74491I.
51
52
53
54
55
56
57
58
59
60

- 1
2
3
4 (37) Intaniwet, A.; Mills, C. A.; Shkunov, M.; Thiem, H.; Keddie, J. L.; Sellin, P. J.
5 Characterization Of Thick Film Poly(Triarylamine) Semiconductor Diodes For Direct X-
6 Ray Detection. *J. Appl. Phys.* **2009**, 106, 064513.
7
8
9 (38) Ankah, G. N.; Büchele, P.; Poulsen, K.; Rauch, T.; Tedde, S. F.; Gimmler, C.;
10 Schmidt, O.; Kraus, T. Pbs Quantum Dot Based Hybrid-Organic Photodetectors For X-
11 Ray Sensing. *Org. Electron.* **2016**, 33, 201–206.
12
13
14 (39) Yakunin, S.; Sytnyk, M.; Kriegner, D.; Shrestha, S.; Richter, M.; Matt, G. J.; Azimi,
15 H.; Brabec, C. J.; Stangl, J.; Kovalenko, M. V.; Heiss, W. Detection Of X-Ray Photons
16 By Solution-Processed Lead Halide Perovskites. *Nat. Photonics* **2015**, 9, 444–449.
17
18
19 (40) Wei, H.; Fang, Y.; Mulligan, P.; Chuirazzi, W.; Fang, H.-H.; Wang, C.; Ecker, B. R.;
20 Gao, Y.; Loi, M. A.; Cao, L.; Huang, J. Sensitive X-Ray Detectors Made Of
21 Methylammonium Lead Tribromide Perovskite Single Crystals. *Nat. Photonics* **2016**, 10,
22 333–339.
23
24
25 (41) Lai, S.; Cosseddu, P.; Basiricò, L.; Ciavatti, A.; Fraboni, B.; Bonfiglio, A. A Highly
26 Sensitive, Direct X-Ray Detector Based On A Low-Voltage Organic Field-Effect
27 Transistor. *Adv. Electron. Mater.* **2017**, 3, 1600409.
28
29
30 (42) Wei, W.; Zhang, Y.; Xu, Q.; Wei, H.; Fang, Y.; Wang, Q.; Deng, Y.; Li, T.;
31 Gruverman, A.; Cao, L.; Huang, J. Monolithic Integration Of Hybrid Perovskite Single
32 Crystals With Heterogenous Substrate For Highly Sensitive X-Ray Imaging. *Nat.*
33 *Photonics* **2017**, 11, 315–321.
34
35
36 (43) Pan, W.; Wu, H.; Luo, J.; Deng, Z.; Ge, C.; Chen, C.; Jiang, X.; Yin, W.-J.; Niu, G.;
37 Zhu, L.; Yin, L.; Zhou, Y.; Xie, Q.; Ke, X.; Sui, M.; Tang, J. Cs₂AgBiBr₆ Single-
38 Crystal X-Ray Detectors With A Low Detection Limit. *Nat. Photonics* **2017**, 11, 726–
39 732.
40
41
42
43 (44) Ciavatti, A.; Cramer, T.; Carroli, M.; Basiricò, L.; Fuhrer, R.; De Leeuw, D. M.;
44 Fraboni, B. Dynamics Of Direct X-Ray Detection Processes In High-Z Bi₂O₃
45
46
47
48
49
50
51
52
53
54
55
56
57
58
59
60

- 1
2
3 Nanoparticles-Loaded PFO Polymer-Based Diodes. *Appl. Phys. Lett.* **2017**, 111,
4 183301.
5
6
7
8 (45) Kasap, S. O. X-Ray Sensitivity Of Photoconductors: Application To Stabilized a-Se. *J.*
9 *Phys. D. Appl. Phys.* **2000**, 33, 2853–2865.
10
11
12 (46) Won, J. H.; Kim, K. H.; Suh, J. H.; Cho, S. H.; Cho, P. K.; Hong, J. K.; Kim, S. U.
13 The X-Ray Sensitivity Of Semi-Insulating Polycrystalline Cdznte Thick Films. *Nucl.*
14 *Instruments Methods Phys. Res. Sect. A Accel. Spectrometers, Detect. Assoc.*
15 *Equip.* **2008**, 591, 206–208.
16
17
18 (47) Oh, K. M.; kim, D. K.; Shin, J. W.; Heo, S. U.; Kim, J. S.; Park, J. G.; Nam, S. H.
19 Measurement Of The Electrical Properties Of A Polycrystalline Cadmium Telluride For
20 Direct Conversion Flat Panel X-Ray Detector. *J. Instrum.* **2014**, 9, P01010–P01010.
21
22
23 (48) Kingsley, J. W.; Weston, S. J.; Lidzey, D. G. Stability Of X-Ray Detectors Based On
24 Organic Photovoltaic Devices. *IEEE J. Sel. Top. Quantum Electron.* **2010**, 16, 1770–
25 1775.
26
27
28 (49) Schafferhans, J.; Baumann, A.; Wagenpfahl, A.; Deibel, C.; Dyakonov, V. Oxygen
29 Doping Of P3HT:PCBM Blends: Influence On Trap States, Charge Carrier Mobility And
30 Solar Cell Performance. *Org. Electron.* **2010**, 11, 1693–1700.
31
32
33 (50) Bracher, C.; Yi, H.; Scarratt, N. W.; Masters, R.; Pearson, A. J.; Rodenburg, C.;
34 Iraqi, A.; Lidzey, D. G. The Effect Of Residual Palladium Catalyst On The Performance
35 And Stability Of PCDTBT:PC70BM Organic Solar Cells. *Org. Electron.* **2015**, 27, 266–
36 273.
37
38
39
40
41
42
43
44
45
46
47
48
49
50
51
52
53
54
55
56
57
58
59
60

ToC figure

